Journal of Statistical Physics, Vol. 125, Nos. 5/6, December 2006 (© 2006)
DOI: 10.1007/s10955-006-9107-x

Patterns and Symmetries in the Visual Cortex and in Natural Images

Ha Youn Lee[1] and Mehran Kardar[2]

Received July 19, 2006; accepted March 30, 2006
Published Online: May 3, 2006

As borders between different entities, lines are an important element of natural images. Indeed, the neurons of the mammalian visual cortex are tuned to respond best to lines of a given orientation. This preferred orientation varies continuously across most of the cortex, but also has vortex-like singularities known as pinwheels. In attempting to describe such patterns of orientation preference, we are led to consider underlying rotation symmetries: Oriented segments in natural images tend to be collinear; neurons are more likely to be connected if their preferred orientations are aligned to their topographic separation. These are indications of a reduced symmetry requiring joint rotations of both orientation preference and the underlying topography. This is verified by direct statistical tests in both natural images and in cortical maps. Using the statistics of natural scenes we construct filters that are best suited to extracting information from such images, and find qualitative similarities to mammalian vision.

KEY WORDS: Visual cortex; Orientational preference map; Pinwheel structure; Joint rotational symmetry; Transversality; Information optimization.

PACS 84.35+i, 89.70.+c, 87.57.Nk

1. INTRODUCTION

The pioneering studies of Hohenberg and Langer have helped us appreciate the origin and ubiquity of patterns in non-equilibrium physical systems.[1,2] They have shown that asking the right questions about the formation and characteristics of patterns can lead to fundamental insights about underlying mechanisms. In this

[1] Theoretical Biology and Biophysics Group, MS-K710, Los Alamos National Laboratory, Los Alamos, NM 87545, USA; e-mail: hayoun@lanl.gov
[2] Department of Physics, Massachusetts Institute of Technology, Cambridge, Massachusetts 02139, USA

paper, we shall apply these lessons to an example from the realm of biological systems, namely certain patterns observed in the mammalian visual cortex. We find that general concepts of symmetry and universality can indeed be useful in this context.

The first step in vision is the focusing of light by the lens of the eye to the retina. The impinging light excites the photoreceptors and in turn activates the different types of retinal neurons.[3] The signal from the roughly one million ganglion cells (the output neurons of the retina) is then accumulated and transmitted through the optic nerve. There is one synapse of processing in the area of thalamus known as the lateral geniculate nucleus (LGN), before the information is transmitted to the primary visual cortex (V1). V1 is the first area of the cortex that processes visual information; in humans it has an area of roughly $13\,\mathrm{cm}^2$.

The electrical activity of individual neurons (typically a train of spikes) can be probed using fine micro-electrodes. The *receptive field* of the neuron refers to the stimuli that elicit the largest response. For example, ganglion cells at a specific spot on the retina respond when a light impinges near that location (topographic organization). However, their response is unlike a photographic film in that they don't fire spikes when there is uniform illumination. The typical receptive field of retinal neurons has a so-called center-surround character, i.e. the maximum firing rate is obtained when a central portion is illuminated while the surrounding area is dark (or vice versa).

The topographic organization of the retina is preserved in both the thalamus and in V1, and one can identify a (distorted) two dimensional map of the visual field in these areas. However, the receptive fields are different: Neurons in the LGN still have a center-surround response similar to their retinal counterparts, while neurons in V1 respond best to bars of lights of a particular orientation. Hubel and Wiesel[4] who originally discovered the orientation preference of V1 neurons, suggested that this could arise if several neurons from LGN were connected to a single neuron in V1. If the former are arranged along a line in the topographic space, the V1 cell will receive its highest input when a bar of light is aligned with the LGN neurons. Such a feed-forward model has since become a paradigm for how information is processed in the brain, gradually becoming more specialized at higher cortical areas.

While micro-electrodes provide information at the scale of a single neuron, it is also possible to obtain information at the scale of the whole cortex using optical imagining methods (dyes changing color due to metabolic byproducts of firing neurons).[5] Intricate maps of global patterns of orientation preference (OP) over the cortex have been obtained in this manner. In the mammalian cortex, the preferred orientation of neurons varies continuously across most of the cortex, but there are prominent pinwheel centers around which all orientations are present. The two possible directions of circulation give two types of pinwheels which occur

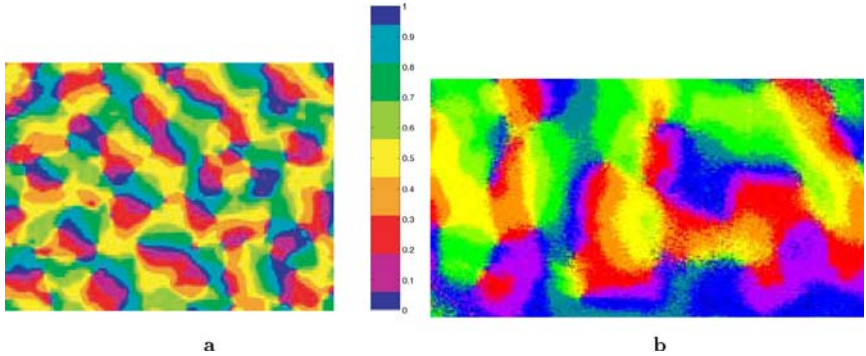

Fig. 1. Orientation preference maps for (a) monkey (provided by K. Obermeyer) and (b) cat (provided by M. Sur and J. Schummers). The different orientations are labeled by colors (central bar). Pinwheel singularities are present in both maps. (color online)

in equal numbers. Two such maps, from monkey and cat respectively, are depicted in Fig. 1.

While the above context may be unfamiliar to the physics audience, the types of patterns presented in this figure certainly have much in common with those observed in magnets and liquid crystals. The discussion of the patterns and symmetries in the remainder of this paper follows these familiar examples. In Section 2 we focus on the dynamics of the topological defects (pinwheels or vortices) in the two dimensional field of OP. We find that rotational symmetries are essential to understanding the fate of topological defects: In systems where the orientations can be rotated independently of the underlying topography the pinwheels tend to annihilate, but they survive when the two rotations must occur together. This is supported by calculating the density of defects in the linear regime (from a superposition of Gaussian modes), and numerical simulations of non-linear models.[6]

Section 3 presents the results of statistical analysis of images of an orientation field. In the first part we analyze OP maps of monkey and cat, and find evidence of the coupling of rotations to the underlying topography. Of course, the necessity of joint-rotations is evident from casual consideration of natural images. In Section 3.2 we quantify this by examining Fourier transforms of lines from a database of natural images. In particular, we emphasize that the transverse component of the power spectrum is larger than the longitudinal one. In the final section, we inquire about the implications of the observed statistics for efficient processing of visual data. Specifically, we construct filters that maximize the information content of the processed visual signal. We find that such optimal filters (a) can account for qualitative features of horizontal connections in V1; and (b) are good for filling in missing gaps in images of lines.

2. PINWHEELS IN EVOLVING ORIENTATION FIELDS

2.1. Evolving Fields

Analytical understanding of the development of visual maps, and its connections to other problems in pattern formation, is best obtained in terms of *evolving fields*. In this framework, OP is modelled by a director field $\mathbf{s} \equiv (s_x(x, y), s_y(x, y))$, indicating the preferred orientation at location $\mathbf{r} \equiv (x, y)$ on the cortex. The field $\mathbf{s}(\mathbf{r}, t)$ then evolves in time according to some development rule that depends on its configurations at earlier times.[7,8] Wolf and Geisel (WG) have shown[9] that a large number of such evolutions can be summarized through a dynamical equation $\partial_t \mathbf{s}(\mathbf{r}, t) = F[\mathbf{s}]$. (WG combine the two components into a single complex field $z = (s_x + is_y)^2$.) Common elements in models of evolving fields are:

(a) Starting from an initial condition with little OP, there is a rapid onset of selectivity governed by $L[\mathbf{s}]$, the *linear* part of the functional $F[\mathbf{s}]$. The characteristic length scale observed in cortical maps is implemented by a linear operator that causes maximal growth of features of wavelength Λ, *i.e.* acting as a 'band-pass filter' in the parlance of circuits. It is possible to follow the linear development analytically: WG show that the density of pinwheels (zeros of the field $z(\mathbf{r})$) has to be larger than π/Λ^2 in this regime.

(b) Since the linear evolution leads to unbounded growth of OP, nonlinearities are essential for a proper saturation of the field. While analytical studies of nonlinear development are difficult, numerical simulations indicate that the OP patterns continue to change (albeit more slowly) even after their magnitudes have saturated. More importantly, the pinwheels typically annihilate in pairs, giving way to a rainbow pattern of wavelength Λ. To maintain pinwheels, development has to be stopped, or extrinsic elements such as inhomogeneities that trap the pinwheels have to be introduced.[10] Since the neural processes that lead to OP are still not fully understood, the stability of pinwheels has not been a topic of much study among neuroscientists. Nevertheless, the search for intrinsically stable pinwheel patterns has motivated some recent studies.[11,12] We propose here an alternative explanation, demonstrating that evolving field models with proper rotational symmetry generically lead to patterns with stable pinwheels.

2.2. Symmetries and Linear Dynamics

Symmetry considerations are paramount in problems of pattern formation. Since all directions are more or less equally present in cortical maps, practically all models of OP (certainly those summarized in WG) assume that different orientations are equivalent.[13] This is implemented by requiring the evolution

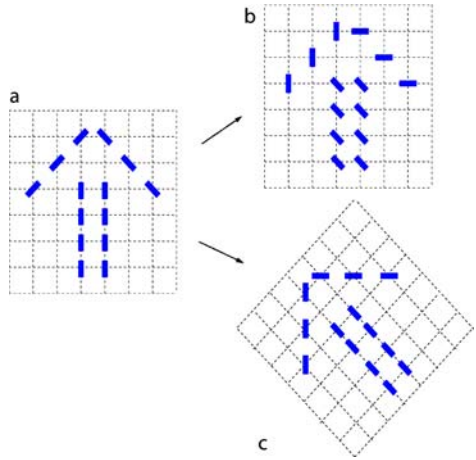

Fig. 2. (a) The image of an arrow formed by oriented solid lines, on a topographic grid of dotted lines. (b) Each solid line is rotated anti-clockwise by 45° independent of the grid. The thus 'rotated' image bears little resemblance to the original. (c) Simultaneous rotation of the grid and the solid lines, as the whole image is rotated. (color online)

of $\mathbf{s}(\mathbf{r}, t)$ to be unchanged if all angles are rotated together. This rotation is independent of the topographic space $\mathbf{r}$, which is also assumed to be isotropic (no preferred directions). Two versions of rotation are illustrated in Fig. 2. Figure 2(b) displays a collection of oriented lines that are rotated independently of the background grid from Fig. 2(a). We propose that the appropriate symmetry for OP maps is simultaneous rotations of the orientations *and* the underlying space, as illustrated in Fig. 2(c).

We believe that the restriction to joint rotation symmetry is an essential aspect of the OP maps, and should be incorporated into models and analytical studies. To underscore the difference between the two symmetries, let us consider the *linear evolution* of the Fourier modes $\tilde{s}_\alpha(\mathbf{q}, t) = \int d^2x e^{i\mathbf{q}\cdot\mathbf{x}} s_\alpha(\mathbf{x}, t)$, where $\alpha = 1, 2$ (or x, y) labels the two components of the vector $\tilde{\mathbf{s}}$. Rotation symmetries constrain the linear evolution to the form

$$\partial_t \tilde{s}_\alpha(\mathbf{q}, t) = \sum_{\beta=1,2} [J(q)\delta_{\alpha\beta} + q_\alpha q_\beta K(q)]\tilde{s}_\beta(\mathbf{q}, t). \tag{1}$$

Due to the assumed isotropy, the functions J and K only depend on the magnitude of the vector $\mathbf{q}$. (For example, they can be band-pass filters peaked at $\overline{q} = 2\pi/\Lambda$, to reproduce the power spectrum of cortical maps.) If rotations of $\mathbf{s}$ and $\mathbf{r}$ are independent, the only possible isotropic tensor is $\delta_{\alpha\beta}$, and the second term must be absent ($K(q) = 0$). However, if $\mathbf{s}$ and $\mathbf{r}$ can only be rotated together, $q_\alpha q_\beta$ is

another possible rank two tensor. (Another way to see this is that $\mathbf{q} \cdot \tilde{\mathbf{s}}$ is invariant under joint rotations, but not separate rotations of $\tilde{\mathbf{s}}$ and $\mathbf{r}$.)

A finite $K(q)$ mixes the evolution of the two components $\tilde{\mathbf{s}}_1$ and $\tilde{\mathbf{s}}_2$. This mixing can be removed by decomposing the field $\tilde{\mathbf{s}}$ into *longitudinal* and *transverse* components. For a given $\mathbf{q}$, the longitudinal component is parallel to $\mathbf{q}$, and the transverse component is perpendicular to it. Under the action of the linear operator in Eq. (1), the two components grow as $e^{[J(q)+q^2K(q)]t}$ and $e^{J(q)t}$. If $K(q) = 0$ (full rotation symmetry) the two modes grow at the same rate. In particular, an equal superposition to the two modes is compatible with a rainbow pattern which does not contain any nodes. (The rainbow is unique among the many possible superposition patterns in that it contains no pinwheels. It is precisely this feature that makes it a likely candidate to survive in the non-linear regime.) However, $K(q)$ is generically non-zero for a joint rotation symmetry, and one of the two modes eventually dominates the other. The dominance of transverse or longitudinal components increases the density of zeros. Unlike the rainbow pattern for $K(q) = 0$, it is not possible to find any superposition of modes in this case which has a uniform amplitude in space.

2.3. Simulations of Non-Linear Dynamics

The arguments from the linear regime strongly suggest that joint rotational symmetry promotes pinwheel stability. To bolster this hypothesis, we carried out simulations of the nonlinear evolution where variables $\{\mathbf{s}_i(t)\}$ were placed on lattice points $\mathbf{r}_i$, and evolved in time according to

$$\partial_t \mathbf{s}_i = \mathbf{s}_i(1 - |\mathbf{s}_i|^2) + \sum_j [J(r_{ij})\, \mathbf{s}_j + K(r_{ij})\, (\mathbf{s}_j \cdot \hat{\mathbf{r}}_{ij})\hat{\mathbf{r}}_{ij}], \tag{2}$$

where $\mathbf{r}_{ij} = \mathbf{r}_i - \mathbf{r}_j$ has magnitude r_{ij} along the unit vector $\hat{\mathbf{r}}_{ij}$. The above equation and similar evolution models are very much in the spirit of the Swift–Hohenberg equation,[1,14] where symmetry plays a key role in modeling pattern formation. The nonlinearity appearing in the first term on the right hand side stabilizes the magnitude of $\mathbf{s}_i$ to unity. The linear evolution is governed by a *vectorial center-surround filter*, composed of two parts: (a) A standard center-surround filter with positive couplings J_s in a circle of size $R/2 \sim \Lambda$ and negative values J_l in an annulus from $R/2$ to R. (b) Additional couplings in the annular region that explicitly depend on orientations relative to the lines joining lattice points, and invariant only under joint rotations. We employ only positive long-range couplings K, to mimic the preferential 'horizontal' connectivity of co-oriented co-axially aligned receptive fields, as reported in Ref. 16. (Similar kinds of anisotropic interactions were also employed in a model for dynamics of neural activity in the visual cortex.[17])

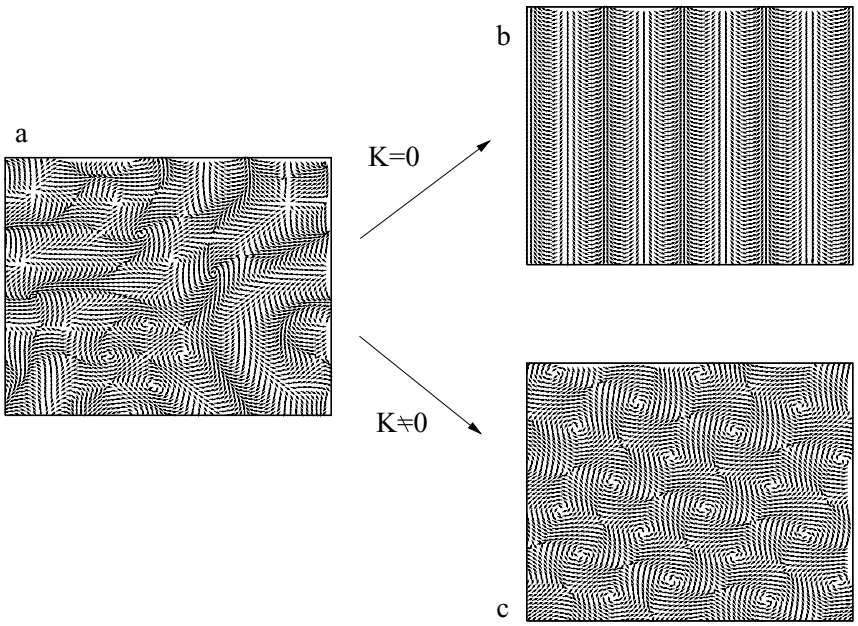

Fig. 3. (a) The development of a random initial condition by a typical center-surround (bandpass) filter leads to a collection of pinwheels. The filter used in (b) has full rotation symmetry ($K(r) = 0$ in Eq. (2)). In this case the pinwheels annihilate in pairs, giving way to a rainbow pattern at long times. (c) By contrast, a model with joint rotation symmetry evolves to a stable pattern of pinwheels. This figure was generated by the *vectorial center-surround* filter in Eq. (2), with a non-zero $K(r)$.

Simulations are started on an $L \times L$ lattice with initial values of $|\mathbf{s}_i| = 10^{-3}$, equally distributed over all angles, with $J_s = 0.01$, $J_l = -0.0034$, and $R = 10$. As shown in Fig. 3(a), undifferentiated initial conditions quickly develop into a pattern with pinwheels reminiscent of actual maps. Further evolution depends on the symmetry of development rules. Full rotation symmetry with $K = 0$, and the action of (b) above turned off, leads in a rainbow state with no pinwheels at long times, as in Fig. 3(b). However, reduction of this symmetry by adding interactions in (b) with $K = 0.0034$, above eventually results in a square lattice of pinwheels, as in Fig. 3(c). Naturally, we do not imply that pinwheels in cortical maps form a square lattice (various inhomogeneities could easily trap these vortices in a distorted arrangement), but that they are intrinsically stable under such development rules.

The precise choice of long-range coupling is not important for the stability of pinwheels. We tested a variety of long-range interactions in our numerical simulations, and found that pinwheels are generally present in the presence of *anisotropy*. As an example, we observe a pinwheel pattern with a negative value

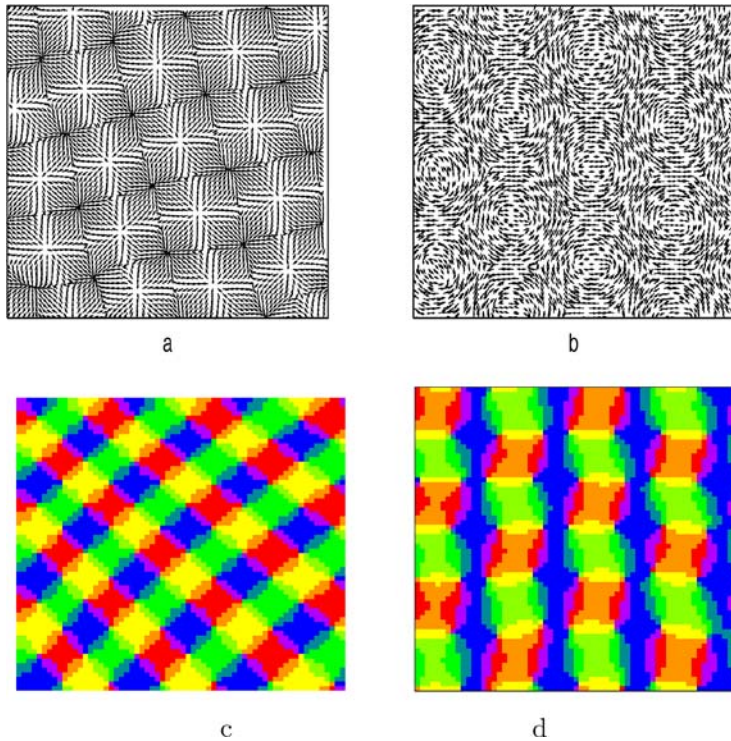

Fig. 4. (a and c) Stable pattern of pinwheels with joint rotation symmetry, with a negative value of $K = -0.0039$. (Compare with Fig. 3c of the manuscript.) (b and d) A pinwheel pattern is also generated in simulations with the model in Eq. (3), which is explicitly invariant under changing the signs of $\mathbf{s}_i$ or $\mathbf{s}_j$. (color online)

of K which is used to generate the map in Fig. 4(a). Another potential concern is that in our simulations the orientations are represented by a *vector*, while in actuality they should be modelled by a *director* field (vectors without arrows). To address this issue, we also consider the following evolution equation

$$\partial_t \mathbf{s}_i = \mathbf{s}_i(1 - |\mathbf{s}_i|^2) + \sum_j \left[J(r_{ij})(\mathbf{s}_i \cdot \mathbf{s}_j)\mathbf{s}_j + K(r_{ij})(\mathbf{s}_j \cdot \hat{\mathbf{r}}_{ij})^2(\mathbf{s}_i \cdot \hat{\mathbf{r}}_{ij})\hat{\mathbf{r}}_{ij} \right]. \quad (3)$$

which is explicitly invariant under rotation of orientations by π. Figure 4(b) displays the result of a corresponding simulation (for interaction strength $K = 0.0034$). The pattern of stable pinwheels is similar to Fig. 3(c), indicating that this is not an artifact of the vectorial model.[18]

2.4. Density of Pinwheels

It is in fact possible to analytically calculate the density of vortices in the linear regime. The key observation is that in this regime the probability distribution for $\vec{S} \equiv (S_x(x,y), S_y(x,y))$ is Gaussian. The most general Gaussian weight subject to joint rotational invariance of $\vec{S}$ and $\vec{r}$, is

$$p\left[\vec{S}\right] \propto \exp\left\{-\frac{1}{2}\int \frac{d^2q}{(2\pi)^2} S_\alpha(\vec{q}\,) S_\beta(-\vec{q}\,)\left[\lambda^{-1}(q)\frac{q_\alpha q_\beta}{q^2} + \tau^{-1}(q)\left(\delta_{\alpha\beta} - \frac{q_\alpha q_\beta}{q^2}\right)\right]\right\}, \tag{4}$$

where $\vec{S}(\vec{q}\,)$ is the Fourier transform of $\vec{S}(\vec{r}\,)$, $\lambda(q)$ and $\tau(q)$ are longitudinal and transverse contents of the power spectrum, and $\tau(q) = \lambda(q)$ in an isotropic system. The average density of zeros is obtained from[20]

$$n = \langle \delta^2(\vec{S}\,) \det \partial_\alpha S_\beta \rangle = \langle \delta^2(\vec{S}(0))\rangle \langle |\partial_x S_x(0)\partial_y S_y(0) - \partial_x S_y(0)\partial_y S_x(0)|\rangle. \tag{5}$$

Here the average can be taken at $\vec{r} = 0$ because of translation symmetry. Also, the averages $\partial_\alpha \vec{S}$ are independent since the probability distribution function is invariant under $\vec{S} \to \vec{S} + \vec{C}$. The first average is easily calculated as

$$\langle \delta^2(\vec{S}(0))\rangle = \int \frac{d^2k}{(2\pi)^2}\left\langle e^{i\vec{k}\cdot\vec{S}(0)}\right\rangle = \int \frac{d^2k}{(2\pi)^2} \exp[-\frac{k^2}{2}\langle \vec{S}(0)\cdot\vec{S}(0)\rangle]. \tag{6}$$

The variance of $\vec{S}(0)$ is

$$\begin{aligned}\langle \vec{S}(0)\cdot\vec{S}(0)\rangle &= \int \frac{d^2q d^2q'}{(2\pi)^4}\langle S_\alpha(\vec{q}\,) S_\alpha(\vec{q}\,')\rangle \\ &= \int \frac{d^2q d^2q'}{(2\pi)^4}(2\pi)^2\delta^2(\vec{q} + \vec{q}\,')\ [\lambda(q) + \tau(q)]\,,\end{aligned} \tag{7}$$

and by inserting Eq. (7) to Eq. (6), we get

$$\langle \delta^2(\vec{S})\rangle = \frac{1}{2\pi}\frac{1}{\int \frac{d^2q}{(2\pi)^2}[\lambda(q) + \tau(q)]} = \frac{1}{\int dq\ q\ [\lambda(q) + \tau(q)]}. \tag{8}$$

As a first step to calculating the average determinant, we consider

$$\begin{aligned}\langle \partial_i S_\alpha(0)\partial_j S_\beta(0)\rangle &= \int \frac{d^2q}{(2\pi)^2}\frac{d^2q'}{(2\pi)^2}(iq_i)(iq'_j)\left\langle S_\alpha(\vec{q}\,) S_\beta(\vec{q}\,')\right\rangle \\ &= \int \frac{d^2q}{(2\pi)^2} q_i q_j \left[\lambda(q)\frac{q_\alpha q_\beta}{q^2} + \tau(q)\left(\delta_{\alpha\beta} - \frac{q_\alpha q_\beta}{q^2}\right)\right] \\ &= \int \frac{d^2q}{(2\pi)^2} q^2 \left[\tau(q)\left(\frac{\delta_{ij}\delta_{\alpha\beta}}{2} - \frac{\delta_{ij}\delta_{\alpha\beta} + \delta_{i\alpha}\delta_{j\beta} + \delta_{i\beta}\delta_{j\alpha}}{8}\right)\right.\end{aligned}$$

$$+\lambda(q)\frac{\delta_{ij}\delta_{\alpha\beta}+\delta_{i\alpha}\delta_{j\beta}+\delta_{i\beta}\delta_{j\alpha}}{8}\Bigg]$$
$$=\frac{\delta_{ij}\delta_{\alpha\beta}}{4\pi}\int dqq^3\tau(q)+\frac{\delta_{ij}\delta_{\alpha\beta}+\delta_{i\alpha}\delta_{j\beta}+\delta_{i\beta}\delta_{j\alpha}}{16\pi}$$
$$\times\int dqq^3\left(\lambda(q)-\tau(q)\right). \tag{9}$$

We next rewrite Eq. (9) as

$$\left\langle\partial_i S_\alpha\partial_j S_\beta\right\rangle=\delta_{ij}\delta_{\alpha\beta}\,\kappa+\left(\delta_{ij}\delta_{\alpha\beta}+\delta_{i\alpha}\delta_{j\beta}+\delta_{i\beta}\delta_{j\alpha}\right)\mu, \tag{10}$$

where $\kappa=\int dq\ q^3\ \tau(q)/(4\pi)$, and $\mu=\int dq\ q^3\ (\lambda(q)-\tau(q))/(16\pi)$ is zero in an isotropic system. In the isotropic system, each of the four derivatives is an independent variable. However, for $\mu\neq 0$, there are two correlated pairs $(\partial_x S_x,\,\partial_y S_y)$, and $(\partial_x S_y,\,\partial_y S_x)$. For the first pair, we have $\langle(\partial_x S_x)^2\rangle=\langle(\partial_y S_y)^2\rangle=\kappa+3\mu$, while for the second pair $\langle(\partial_y S_x)^2\rangle=\langle(\partial_x S_y)^2\rangle=\kappa+\mu$. The cross correlations in each pair are identical, $\langle\partial_x S_x\partial_y S_y\rangle=\langle\partial_x S_y\partial_y S_x\rangle=\mu$, such that the average value of the determinant is zero.

As a second step towards the calculation of average absolute value of the determinant, we find its probability distribution as

$$p(d)=\left\langle\delta\left[d-\left(\partial_x S_x\partial_y S_y-\partial_x S_y\partial_y S_x\right)\right]\right\rangle=\int\frac{d\omega}{2\pi}e^{i\omega d}\left\langle e^{i\omega(\partial_x S_x\partial_y S_y-\partial_x S_y\partial_y S_x)}\right\rangle. \tag{11}$$

As established above, the two factors in the final exponent are independent random elements. The random variables $\partial_\alpha S_\beta\equiv u_{\alpha\beta}$ are Gaussian distributed, with covariances given by Eq. (10). By inverting the co-variance matrix, we can construct the probability distribution for $\{u_{\alpha\beta}\}$, and then calculate the average

$$\left\langle e^{i\omega u_{xx}u_{yy}}\right\rangle=\int\frac{du_{xx}du_{yy}}{\mathcal{N}}$$
$$\times\exp\left\{-\frac{1}{2}(u_{xx},u_{yy})\begin{bmatrix}\frac{\kappa+\mu}{(\kappa+\mu)^2-\mu^2} & -\frac{\mu}{(\kappa+\mu)^2-\mu^2}-i\omega\\ -\frac{\mu}{(\kappa+\mu)^2-\mu^2}-i\omega & \frac{\mu}{(\kappa+\mu)^2-\mu^2}\end{bmatrix}\begin{pmatrix}u_{xx}\\ u_{yy}\end{pmatrix}\right\}$$
$$=\left[\frac{(\kappa+\mu)^2}{((\kappa+\mu)^2-\mu^2)^2}-\frac{\mu^2}{((\kappa+\mu)^2-\mu^2)^2}-\frac{2i\omega\mu}{(\kappa+\mu)^2-\mu^2}+\omega^2\right]^{-\frac{1}{2}}$$
$$\times\left[\frac{(\kappa+\mu)^2-\mu^2}{((\kappa+\mu)^2-\mu^2)^2}\right]^{\frac{1}{2}}$$
$$=\left[1+\omega^2((\kappa+\mu)^2-\mu^2)-2i\omega\mu\right]^{-\frac{1}{2}}. \tag{12}$$

(The normalization $\mathcal{N}$ in the denominator is simply the numerator evaluated at $\omega = 0$.) Similarly, the second average is

$$\left\langle e^{-i\omega u_{xy}u_{yx}} \right\rangle = \left[1 + \omega^2((\kappa + 3\mu)^2 - \mu^2) + 2i\omega\mu\right]^{-\frac{1}{2}}. \tag{13}$$

Inserting Eqs. (12) and (13) into Eq. (11) gives the implicit result

$$p(d) = \int_{-\infty}^{\infty} \frac{d\omega}{2\pi} \frac{e^{i\omega d}}{[1 - 2i\omega\mu + \omega^2(\kappa^2 + 2\mu\kappa)]^{\frac{1}{2}}[1 + 2i\omega\mu + \omega^2(\kappa^2 + 6\mu\kappa + 8\mu^2)]^{\frac{1}{2}}}. \tag{14}$$

Let us consider the isotropic case, $\mu = 0$. The probability distribution function is

$$p(d) = \int_{-\infty}^{\infty} \frac{d\omega}{2\pi} \frac{e^{i\omega d}}{1 + \kappa^2\omega^2} = \frac{1}{2\kappa} e^{-|d|/\kappa}, \tag{15}$$

from which we obtain

$$\langle |d| \rangle = 2\int_0^{\infty} dx \frac{1}{2\kappa} e^{-x/\kappa} = \kappa. \tag{16}$$

From Eqs. (5), (8), and (16), average density of pinwheels is then

$$n = \frac{1}{4\pi} \frac{\int dq q^3 \tau(q)}{\int dq q(\lambda(q) + \tau(q))} = \frac{1}{8\pi} \frac{\int dq q^3 P(q)}{\int dq q P(q)}, \tag{17}$$

where $P(q) = \lambda(q) + \tau(q) = 2\tau(q)$ is the power spectrum of the field. The above result is smaller by a factor of two than that obtained in Ref. 9. However, our calculation was with a vector field, whereas the orientation preference is a director field which is the same if the vector is inverted. To incorporate this feature, Ref. 9 works with a complex field $|z(\vec{x})|e^{2i\theta(\vec{x})} \equiv (S_x + iS_y)^2$, a procedure that doubles the zeros calculated above for the field $(S_x + iS_y)$. This factor is not important to us, since we are interested in how the result is modified by anisotropy.

Performing the integral in Eq. (14) for $\mu \neq 0$ is not an easy task. We note that since $\langle d \rangle = 0$, the average of the absolute value provides a measure of the width of the probability distribution $p(d)$. A similar measure of the width of the distribution that is much easier to calculate is the standard deviation $\sqrt{\langle d^2 \rangle}$. Using standard properties of Gaussian distributed variables, the variance of d is calculated as

$$\begin{aligned}
\langle d^2 \rangle &= \langle (\partial_x S_x \partial_y S_y - \partial_x S_y \partial_y S_x)^2 \rangle \\
&= \langle (\partial_x S_x)^2 \rangle \langle (\partial_y S_y)^2 \rangle + 2\langle \partial_x S_x \partial_y S_y \rangle^2 + \langle (\partial_x S_y)^2 \rangle \langle (\partial_y S_x)^2 \rangle \\
&\quad + 2\langle \partial_x S_y \partial_y S_x \rangle^2 - 2\langle \partial_x S_x \partial_y S_y \rangle \langle \partial_x S_y \partial_y S_x \rangle
\end{aligned}$$

$$= (\kappa + 3\mu)^2 + 2\mu^2 + (\kappa + \mu)^2 + 2\mu^2 - 2\mu^2$$
$$= 2\kappa^2 + 8\mu\kappa + 12\mu^2. \tag{18}$$

As measures of the width of the distribution, $\langle |d| \rangle$ and $\sqrt{\langle d^2 \rangle}$ should vary together. For our estimate, we shall assume that they are proportional, and choose the a proportionality constant that makes the two expression equal for $\mu = 0$; i.e. we make the replacement

$$\langle |d| \rangle \to \sqrt{\frac{\langle d^2 \rangle}{2}} = \sqrt{\kappa^2 + 4\mu\kappa + 6\mu^2}, \tag{19}$$

resulting in the density of zeros

$$n \approx \frac{\sqrt{\kappa^2 + 4\mu\kappa + 6\mu^2}}{\int dq\ q\ (\lambda(q) + \tau(q))}. \tag{20}$$

Using the expressions for κ and μ, we note that

$$\kappa + 2\mu = \frac{1}{4\pi} \int dq\ q^3 \left(\tau(q) + \frac{\lambda(q) - \tau(q)}{2} \right) = \frac{1}{8\pi} \int dq q^3 P(q), \tag{21}$$

where $P(q) \equiv \lambda(q) + \tau(q)$ is the total power content at q. With the aid of Eq. (21), Eq. (20) now becomes

$$n \approx \frac{\sqrt{(\kappa + 2\mu)^2 + (2\mu)^2}}{\int dq\ q\ P(q)} = \frac{1}{8\pi} \frac{\int dq\ q^3\ P(q)}{\int dq\ q\ P(q)} \sqrt{1 + \left[\frac{\int dq\ q^3\ (\lambda(q) - \tau(q))}{\int dq\ q^3\ (\lambda(q) + \tau(q))} \right]^2}. \tag{22}$$

For a fixed $P(q)$, the density of zeros is minimum in the isotropic limit of $\tau(q) = \lambda(q)$. In the extreme anisotropic limit of $\tau(q) = 0$ or $\lambda(q) = 0$, the density of zeros increases by a factor of $\sqrt{2}$. In view of the approximations involved, we also performed numerical simulations to check if the density of pinwheels is higher in the anisotropic case. We found that this is indeed the case although the relative increase in density of 1.12 is less than the value of $\sqrt{2}$.

Let us illustrate the time evolution of the density of zeros, using a simple linear model for development of the field, in which the longitudinal and transverse components of the power spectrum grow as

$$\lambda(q, t) = \lambda_0(q)\, e^{r_l(q)\, t},$$
$$\tau(q, t) = \tau_0(q)\, e^{r_t(q)\, t}, \tag{23}$$

where growth rates are $r_l(q) = 2[J(q) + q^2 K(q)]$ and $r_t(q) = 2J(q)$. If initially $\lambda_0(q) = \tau_0(q) = P_0/2$, for $q < q_{\max}$, i.e., an isotropically random initial condition,

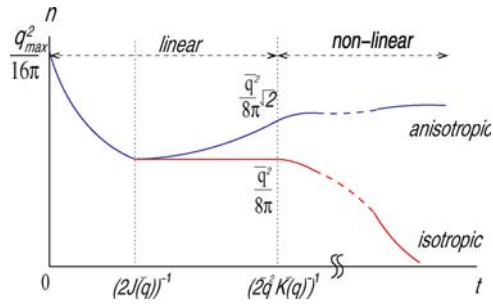

Fig. 5. Schematic depiction of the evolution of the density of zeros for isotropic (red line) and anisotropic (blue line) interactions. Anisotropy results in an increase of the density of pinwheels in the latter stages of linear regime. The non-linear extrapolation is based on simulation results. (color online)

the density of zeros starts as

$$n(t=0) \approx \frac{1}{16\pi} q^2_{\max}. \tag{24}$$

As time goes on, modes with the largest growth rate dominate, reducing n through pair annihilations. Assuming small anisotropy, such that $r_l(q) \approx r_t(q) = 2J(q)$ with a maximum at $\bar{q} = 2\pi/\Lambda$, we have

$$n\left(t \geq (2J(\bar{q}))^{-1}\right) \approx \frac{1}{8\pi}\bar{q}^2 = \frac{\pi}{2\Lambda^2}. \tag{25}$$

However, because of small anisotropy ($r_l(q) \neq r_t(q)$), one of these nearly degenerate modes will dominate the other, such that for longer times,

$$n\left(t \geq (2\bar{q}^2K(\bar{q}))^{-1}\right) \approx \frac{1}{8\pi}\bar{q}^2\sqrt{2} = \frac{\pi}{2\Lambda^2}\sqrt{2}. \tag{26}$$

Figure 5 shows schematic evolution of n for isotropic and anisotropic cases, the increase of the density in the latter must also involve creation of pairs of vortices.

3. STATISTICS OF LINES IN IMAGES

3.1. Analysis of Cortical Maps

In the previous section we were appealing to the stablity of pinwheels to argue that the dynamics of OP must follow a joint rotational symmetry. However, it is indeed possible that the pinwheels are present due to arrested dynamics of a fully symmetric field. (The dynamics may have been stopped due to development, or slowed down by inhomogeneities.) Is it possible to distinguish between these alternatives by direct analysis of cortical patterns such as those reproduced in Fig. 1. This is indeed what we shall argue in this section.

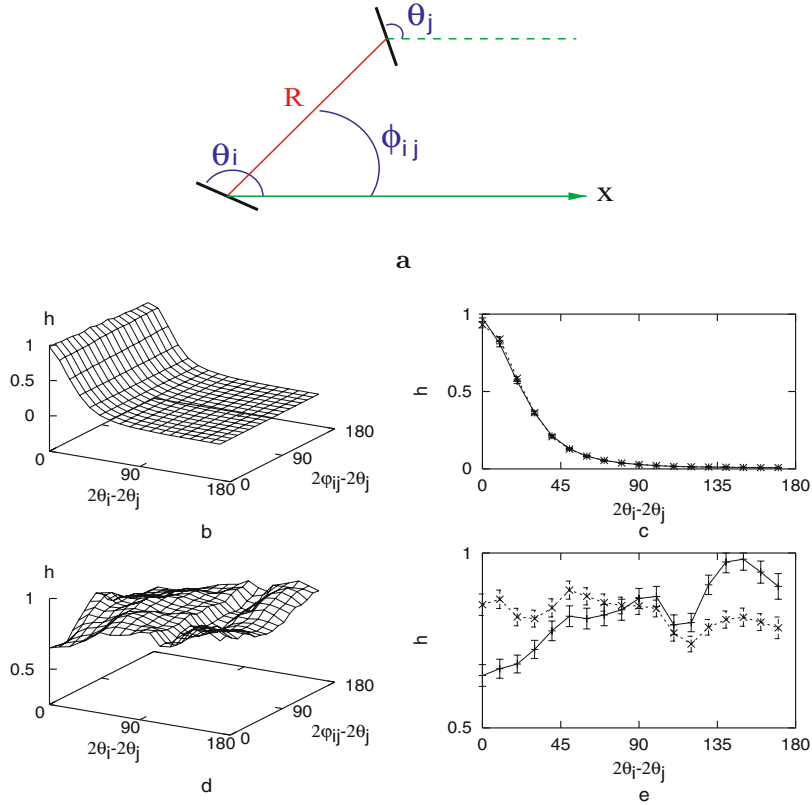

Fig. 6. Histograms of OP from a cortical map of monkey. (a) The relative orientation $2\left(\theta_i - \theta_j\right)$, between two pixels i and j at a distance R, is one argument of the histogram; the second is the OP of one point measured relative to the line joining the two pixels (at angle ϕ_{ij}). Full histograms are shown on the left column, while the right column is for $2\left(\phi_{ij} - \theta_j\right) = 0^0$ (solid line) or 90^o (dotted line). (b and c) are for short separations of 5 to 10 pixel spacings, and show no dependence on the relative angle. By contrast, there is a small but clear indication of a coupling to the underlying topography in (d) and (e) which are taken at distances of 70 to 75 pixels, comparable to the separations of pinwheels. Such dependence indicates the lack of full rotation symmetry in the map. (color online)

To directly test the hypothesis of reduced rotation symmetry, we made joint histograms of the form $h_R\left[2\left(\theta_i - \theta_j\right), 2\left(\phi_{ij} - \theta_j\right)\right]$, where θ_i and θ_j are OPs at two locations i and j separated by a distance R, as indicated in Fig. 6(a). (The factor of two is introduced since the relative orientation is defined i from 0 to π.) The second argument measures the angle relative to the line joining points i and j. If the orientations are independent of topography, the histograms will be independent of their second argument.

Histograms from the map of monkey in Fig. 1(a) (in the form of 360×480 pixels, provided by K. Obermeyer) are shown on the left column in Fig. 6; the right column shows cross-sections at $2\left(\phi_{ij} - \theta_j\right) = 0^\circ$ and 90° which display maximal contrast. Figure 6(b) and (c) are at separations R which are a fraction of the typical distance between pinwheels, and show no indication of any dependence on topography. By contrast, Fig. 6(d) and (e) correspond to values of R comparable to pinwheel separations. There is now a small, but distinct dependence on the orientation of the line between two points; indicating that the OPs do not follow a distribution with full rotational symmetry.

Similar results were obtained for the map from cat in Fig. 1(b) (204×372 pixels, provided by M. Sur and J. Schummers). In neither case is the dependence on the second argument large (at most around %20), and some assessments of its statistical significance is needed. Since we had access to only one map in each case we made an indirect estimate of statistical error by constructing an artificial ensemble of 2000 histograms through random samplings of 2.9% of total pixels in the monkey map. From the thus included errors bars in Fig. 6(e), we conclude that the differences fall outside statistical errors.

3.2. Transversality of Natural Images

An image on a screen is represented by a set of intensities at each pixel. The photoreceptors of the retina also respond to the intensity of light arriving from specific directions. However, when it comes to interpreting the content of an image, primary clues are the borderlines between different regions. As discussed earlier, already at the level of the mammalian primary visual cortex (V1), neurons respond best not to points of light, but to lines of particular orientation.[4] It is thus important to inquire about the statistics of lines in natural scenes, and the implications for vision. In Ref. 21, such a study is performed by first converting images to a set of lines: Correlations of a pair of such lines with their relative location in space, indicates a tendency towards *co-circularity*, namely the most likely arrangement of the two segments is to lie along a circular arc joining them. We start with a similar decomposition of images to lines, examine their statistics (e.g. by Fourier transformation), and explore their implications for visual detection.

There are previous studies of the power spectrum of the (scalar) intensity correlations of natural images.[22,23] For a vectorial quantity, a natural decomposition is into longitudinal/transverse Fourier components, which measure the variations parallel/perpendicular to a wavevector $\vec{k}$. Such decomposition is for example quite common in studies of turbulent velocity fields.[24,25] We construct similar measures of variations of the lines in natural images (which unlike a vector field do not point to a specific direction), and find enhanced power in the orthogonal (transverse) channel. We designate this feature, related to the prevalence of sharp lines, the 'transversality' of natural images.

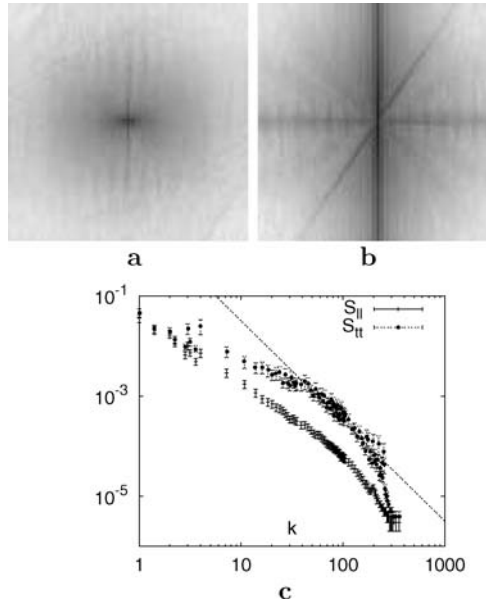

Fig. 7. Intensity plots of the longitudinal $S_{\ell\ell}(\vec{k})$ (a), and transverse $S_{tt}(\vec{k})$ (b), power spectra obtained from averaging over a set of 100 natural images. (c) Log–log plots of $S_{\ell\ell}(k)$ and $S_{tt}(k)$ after averaging over all angles.

Our starting point is a collection of black and white pictures from a database, "http://hlab.phys.rug.nl/imlib/index.html",[26] which includes trees, buildings, flowers, leaves, and grass. The data, which is in the form of a scalar intensity at each pixel, is then converted into oriented segments $[s_x(\vec{X}), s_y(\vec{X})]$ at each pixel $\vec{X}$, using filters based on the second derivative of a Gaussian and its Hilbert transform.[27] Since $[s_x, s_y]$ and $[-s_x, -s_y]$ describe the same orientation, we introduce the tensor field $\mathbf{s}_{\alpha\beta}(\vec{X}) = s_\alpha(\vec{X})s_\beta(\vec{X})$, which is invariant under reflection. The two dimensional Fourier transforms of the components of this tensor lead to a corresponding $\mathbf{S}_{\alpha\beta}(\vec{k})$. The longitudinal and transverse components of the tensor are then obtained as

$$S_\ell(\vec{k}) = tr[\mathbf{L}(\vec{k})\mathbf{S}(\vec{k})],\ S_t(\vec{k}) = tr[\mathbf{T}(\vec{k})\mathbf{S}(\vec{k})], \tag{27}$$

with the aid of the projection operators

$$\mathbf{L}_{\alpha\beta}(\vec{k}) = \hat{k}_\alpha\, \hat{k}_\beta, \quad \mathbf{T}_{\alpha\beta}(\vec{k}) = [\delta_{\alpha\beta} - \hat{k}_\alpha\, \hat{k}_\beta], \tag{28}$$

where $\hat{k}$ is the *unit vector* in the direction of $\vec{k}$.

Figure 7(a) and (b) show the power spectra $S_{\ell\ell}(\vec{k}) \equiv |S_\ell(\vec{k})|^2$ and $S_{tt}(\vec{k}) \equiv |S_t(\vec{k})|^2$ after averaging over 100 images. Clearly these quantities are not isotropic

and vary with angle. This is due to the predominance of vertical and horizontal segments in the images. The bias of oriented segments along cardinal directions in natural scenes is well known,[28] and a similar bias exists in the OPs of cortical maps from adult ferret and cat.[29,30] There is a corresponding larger area of V1 devoted to vertical and horizontal orientations, and a greater stability of cardinal neurons to changes of orientation.[31] Since we are not interested in the predominance of specific orientations, we remove this anisotropy by averaging over rotated images.[32] Equivalently, we can average the power spectra in Fig. 7 over all angles, resulting in $S_{\ell\ell}$ and S_{tt} as a function of $|\vec{k}|$, as depicted in Fig. 7(c).

The data in Fig. 7 clearly shows higher power in the transverse component. The longitudinal power spectrum is reasonably close to a power-law form k^{-2}, indicated by the dotted line in this logarithmic plot. Such a power-law was fitted previously to the power-spectrum obtained from the *intensity* of natural images, and presumably reflects an underlying scale invariance since objects can appear at any distance from the viewer. The transverse power spectrum coincides with the longitudinal one at large values of k; this is expected, reflecting the (imposed) isotropy of line segments at short distances. It is not clear to us, why the two spectra also approach each other at small k (longest wave-lengths); this may be an artifact of the way the images are framed in the pictures.

The enhanced transverse power is a consequence of the abundance of sharp and extended edges in natural images. An elementary illustration is obtained by comparing a long straight line with a horizontal arrangement of short vertical segments as in a fence. The former has no longitudinal Fourier component while the latter has weak transverse character. To see whether there are other sets of images with different character, we did a sampling of paintings from modern art. We find that many paintings from the impressionist school with blurred lines have approximately equal transverse and longitudinal powers, as shown in Fig. 8(a) and (c). By contrast, cubist paintings with sharp lines share (and in fact exceed) the transversality of natural images, as depicted in Fig. 8(b) and (d).[33]

4. IMPLICATIONS FOR VISUAL DETECTION

4.1. Horizontal Connections

Since the task of the visual cortex is to decipher visual signals, its design should incorporate characteristics and correlations from natural images. Within V1 there are *horizontal connections* (extending for 2–5 mm) which mostly link columns of neurons with similar OPs.[34,35] Staining experiments with injected biochemical tracers in the tree shrew reveal that these lateral connections are longer and stronger along an axis in the map of visual field that corresponds to the preferred orientation of the injection site.[16] Similarly, in the cat visual cortex, facilitatory effects occur only between neurons which are co-axial in the

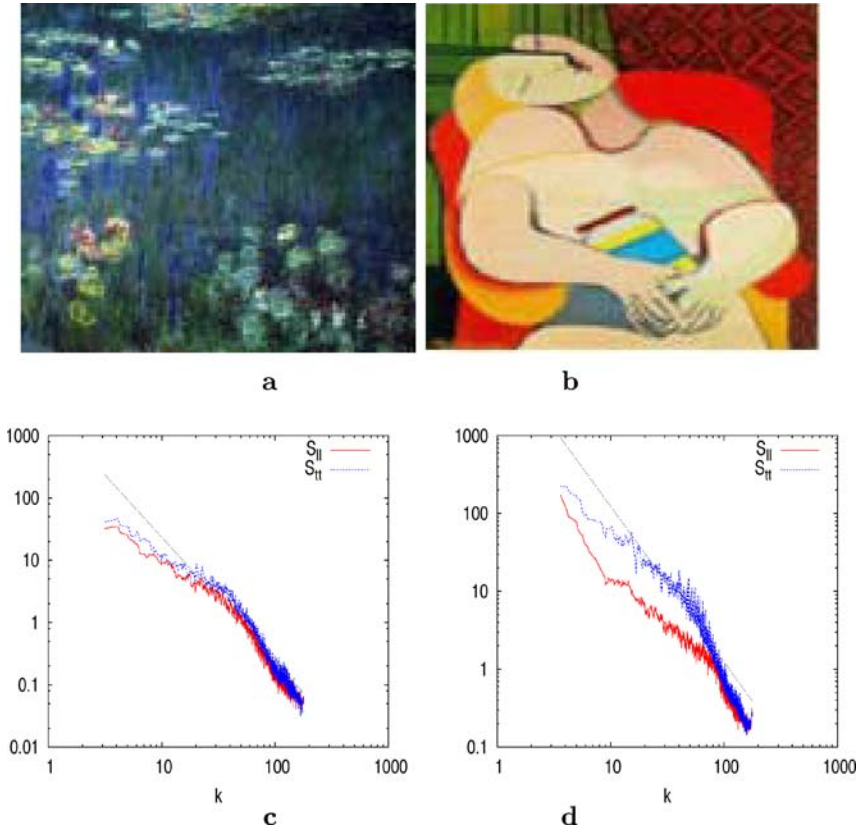

Fig. 8. Monet's Water-lilies (a) and Picasso's The cream (b). The corresponding log–log plots of longitudinal $S_{\ell\ell}(\bar{k})$ and transverse $S_{tt}(\bar{k})$ power spectra appear respectively in (b) and (d). (color online)

spatial domain and co-oriented in the orientation domain.[36] Neural connections of inhibitory cells in V1 also display anisotropic features in OP.[37] Although less understood than the feed-forward connections from LGN, the long range connections in V1 are presumed to mediate the global integration of an image from its local elements. Evidence supporting this comes from fMRI investigations in monkeys and humans: The neurons in V1 show higher response when viewing a long extended line, compared to randomly oriented segments of the line.[38]

We next attempt to relate the statistics of natural images calculated in the previous section to the lateral connections observed between neurons of V1, using information theoretic methods. Indeed, information theory has been used to describe early visual processing, such as the contrast response of large monopolar cells,[39] the 'center surrounded' receptive fields in the retina,[40,41] and the *white*

spatial and temporal power spectrum of signals from the LGN.[41,42] In Ref. 43, linear filters for processing intensity signal inputs to V1 were calculated through maximizing information subject to certain cost functions. Our approach is based on the latter, and as extended in Ref. 44, but employing an input signal which is a vector field.

The response of simple cells in V1 is primarily to an oriented line in a preferred direction, which we shall approximate by $\mathrm{tr}[\mathbf{t}(\vec{x})\mathbf{s}(\vec{X})] = [\vec{t}(\vec{x}) \cdot \vec{s}(\vec{X})]^2$. Here $\mathbf{s}_{\alpha\beta}(\vec{X}) = s_\alpha(\vec{X})s_\beta(\vec{X})$ is constructed from the orientation of the image segment (input signal) at position $\vec{X}$ in the visual field, while a tensor $\mathbf{t}_{\alpha\beta}(\vec{x}) \equiv t_\alpha(\vec{x})t_\beta(\vec{x})$ is defined in terms of the OP of a neuron at location $\vec{x}$ in V1. The topographic map between the visual field and V1 provides a mapping between $\vec{x}$ and $\vec{X}$. However, to emphasize that this mapping is not one to one, with many V1 neurons responding to signals at the same position in the visual field, we use two symbols $\vec{X}$ and $\vec{x}$.[45] Our main interest is in the *lateral connections* to a cell from other neurons in V1. With this aim, we indicate the net response (neuron firing rate), by

$$O(\vec{x}) = \mathrm{tr}[\mathbf{t}(\vec{x})\mathbf{s}(\vec{X})] + \int d^2y F(\vec{x}, \vec{y})\mathrm{tr}[\mathbf{t}(\vec{y})\mathbf{s}(\vec{Y})] + \eta(\vec{x}). \tag{29}$$

The 'filter function' $F(\vec{x}, \vec{y})$ denotes the strength of the horizontal connection between the neurons at $\vec{x}$ and $\vec{y}$; $\eta(\vec{x})$ is the noise experienced by the neuron which is assumed to be uncorrelated at different points, with $\langle \eta(\vec{x})\eta(\vec{x'})\rangle = \sigma^2\delta^2(\vec{x} - \vec{x'})$.

Given the stochastic nature of the input signal (as well as the noise), the output $O(\vec{x})$ is a random variable with a (joint) probability distribution $p[O(\vec{x})]$. The associated Shannon information[46] is

$$I = -\langle \ln p[O(\vec{x})]\rangle \approx \frac{1}{2} \ln \det[\langle O(\vec{x})O(\vec{x'})\rangle_c], \tag{30}$$

where $\langle O(\vec{x})O(\vec{x'})\rangle_c$ is the second cumulant (co-variance) of the output. We can show that subject to reasonable approximations and constraints, the filter function that maximizes the information I, has the form

$$F(\vec{x}, \vec{y}) = \frac{\mathbf{t}_{\alpha\beta}(\vec{x})\mathcal{S}_{\alpha\beta\gamma\delta}(\vec{X} - \vec{Y})\mathbf{t}_{\gamma\delta}(\vec{y})}{C_2(\vec{x} - \vec{y})}. \tag{31}$$

In the above equation, the tensor $\mathbf{t}_{\alpha\beta}(\vec{x}) \equiv t_\alpha(\vec{x})t_\beta(\vec{x})$ encodes the OP of the neuron at $\vec{x}$. The optimal connection strength thus depends on the OP at both end points, and is also proportional to the two point correlation function of the ensemble of input signals $\mathcal{S}_{\alpha\beta\gamma\delta}(\vec{X} - \vec{Y}) = \langle \mathbf{s}_{\alpha\beta}(\vec{X})\mathbf{s}_{\gamma\delta}(\vec{Y})\rangle_c/\sigma^2$ at the corresponding locations and orientations. ($C_2(\vec{x} - \vec{y})$ is the cost of wiring neurons over a distance $|\vec{x} - \vec{y}|$.)

The above form qualitatively agrees with the observations in tree shrew[16] and cat.[36] To confirm that Eq. (31) does indeed predict the enhanced horizontal connections between collinear and co-oriented neurons, we measured the two point correlation functions, $\mathcal{S}_{\alpha\beta\gamma\delta}(\vec{X} - \vec{Y})$, by averaging over a set of five images

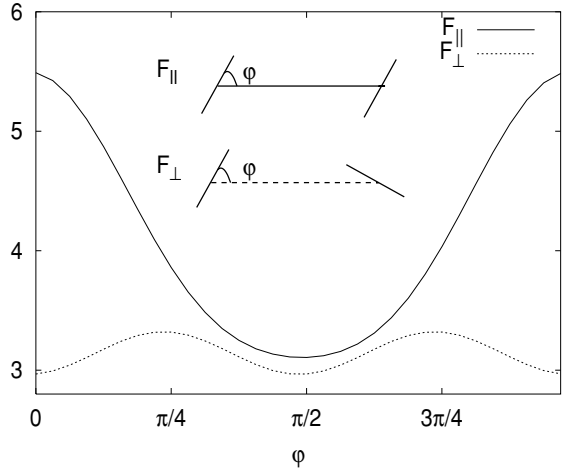

Fig. 9. The strength of horizontal connections among neurons with parallel OPs (solid line $F_{||}$), and with orthogonal OPs (dotted line $F_{\perp}$), as a function of their angle φ to the line between their locations in the visual field. The results are for a fixed separation, and obtained from the statistics of lines, $\mathcal{S}_{\alpha\beta\gamma\delta}(\vec{X}-\vec{Y})$, in a set of five images of trees.

of trees. Figure 9 compares the strength of the connection among neurons with parallel OPs ($F_{\|}$) to that of neurons with orthogonal OPs ($F_{\perp}$), as a function of the angle φ between one of the OPs, and the line joining their locations in the visual field. The figure is for a constant separation $|\vec{x}-\vec{y}|$, the angular dependence is not very sensitive to this separation. There is a strong maximum in $F_{\|}$ at collinearity $\varphi = 0$; while $F_{\perp}$ (which is always smaller than $F_{\|}$) shows weak maxima at $\pi/4$ and $3\pi/4$ (consistent with the co-circularity principle[21]).

4.2. Transverse Filters

One advantage of the above optimal filters is that it enables making up for missing information using the expected statistics of the images. If the primary signal $s_{\alpha}(\vec{X})$ is somehow corrupted, the connections provide a guess based on global statistics. Let us employ similar principles to construct artificial algorithms for visual detection, which (like the human brain) are adept at deducing global shapes in an image composed of edges. We define a *vectorial output* whose components are

$$O_{\alpha}(\vec{x}) = \int d^2y \mathbf{F}_{\alpha\beta}(\vec{x}-\vec{y}) s_{\beta}(\vec{y}) + \eta_{\alpha}(\vec{x}). \tag{32}$$

$$\mathbf{F}_{\alpha\beta}(\vec{k}) = \mathbf{L}_{\alpha\beta}(\vec{k}) F_{\ell}(\vec{k}) + \mathbf{T}_{\alpha\beta}(\vec{k}) F_{t}(\vec{k}). \tag{33}$$

The filter is now a 2×2 matrix. As in Eq. (27) its Fourier transform can be projected into longitudinal/transverse parts as

$$\mathbf{F}_{\alpha\beta}(\vec{k}) = \mathbf{L}_{\alpha\beta}(\vec{k})F_\ell(\vec{k}) + \mathbf{T}_{\alpha\beta}(\vec{k})F_t(\vec{k}). \tag{34}$$

We maximize the information I subject to an appropriate cost function C, including a constraint on the total gain of the filter and a penalty proportional to the mean square spatial extent of the receptive field,[43,44]

$$\begin{aligned} W &= I - C \\ &= \frac{A}{2}\int \frac{d^2k}{(2\pi)^2}\Big[S_{\ell\ell}(\vec{k})|F_\ell(\vec{k})|^2 + S_{tt}(\vec{k})|F_t(\vec{k})|^2 \\ &\quad - \lambda\left(|F_\ell(\vec{k})|^2 + |F_t(\vec{k})|^2\right) \\ &\quad - \mu\left(|\vec{\nabla}_k F_\ell(\vec{k})|^2 + |\vec{\nabla}_k F_t(\vec{k})|^2\right)\Big]. \end{aligned} \tag{35}$$

From Eq. (35), the larger amplitude of $S_{tt}(\vec{k})$ compared to $S_{\ell\ell}(\vec{k})$ leads us $F_\ell(\vec{k}) = 0$. The transverse filter $F_t(\vec{k})$, is the bound solution of the variational equation,

$$\left[S_{tt}(\vec{k}) + \mu\nabla_k^2\right]F_t(\vec{k}) = \lambda F_t(\vec{k}), \tag{36}$$

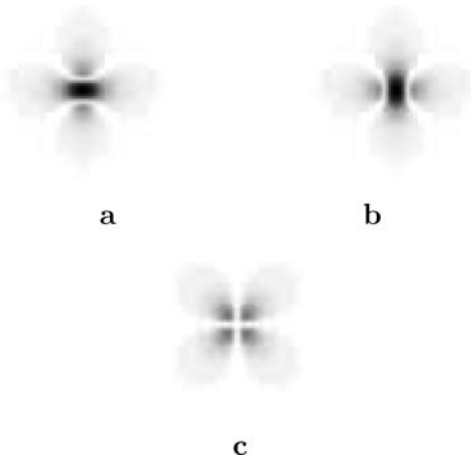

Fig. 10. Optimized filter functions, F_{xx} (a), F_{yy} (b), and F_{xy} (c). Absolute values of F_{xx}, F_{yy}, and F_{xy} are calibrated linearly with the setting of $F_{xx}(0)$ equals 255, the maximum intensity. The anisotropic feature of these filter functions enable efficient sampling of orientation signals statistically correlated with the topographic space.

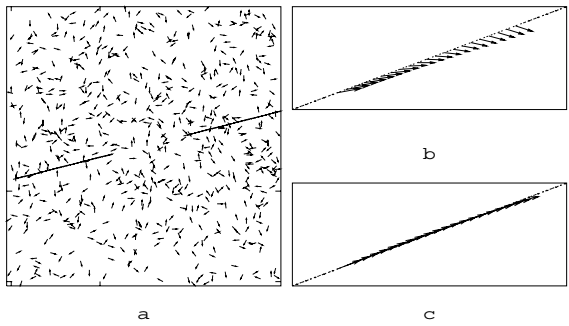

Fig. 11. (a) A test image of a directed line with a gap (plus noise). Reconstructions of the missing segment, with an *isotropic* filter (b); and with a *transverse* filter (c).

where we have $S_{tt}(\vec{k}) \approx A|k|^{-2}$ in the intermediate range of k. After the back transform to real space, we have

$$r^2(1+r^2)\frac{\partial^2 F_t(r)}{\partial r^2} + r(1+5r^2)\frac{\partial F_t(r)}{\partial r} + \left[r^2\left(4+B+\frac{\partial^2}{\partial\phi^2}\right)+\frac{\partial^2}{\partial\phi^2}\right]F_t(r) = 0, \tag{37}$$

where ϕ is the angular variable, $B = A/\mu$, and $r = \sqrt{\mu/\lambda}|\vec{x}|$. If we neglect the angular dependence of $F_t(r)$, $F_t(r)$ behaves as $\exp[-(1+B/4)r^2]$ near the origin and the Fourier transform of $F_t(r)$ is given as

$$F_t(k) = \sqrt{\frac{2\pi}{C}}e^{-\frac{k^2}{4C}}, \tag{38}$$

where $C = 1 + B/4$. Within this approximation, the filter function $F_{\alpha\beta}(\vec{r})$ is

$$F_{\alpha\beta}(\vec{r}) = \frac{r_\alpha r_\beta}{r^2}F_1(r) + \left(\delta_{\alpha\beta} - \frac{r_\alpha r_\beta}{r^2}\right)F_2(r), \tag{39}$$

where $F_1(r) = (1-e^{-Cr^2})/(\sqrt{2\pi C}r^2)$ and $F_2(r) = \sqrt{2C/\pi}\ \ e^{-Cr^2} - F_1(r)$. Figure 10 depicts intensity plots of $F_{xx}(\vec{r})$, $F_{yy}(\vec{r})$, and $F_{xy}(\vec{r})$.

We have compared the performance of the transverse filter with that of the isotropic filter, $F_{\rm iso}(r) = \sqrt{C/\pi}e^{-cr^2}$ from $F_t(\vec{k}) = F_\ell(\vec{k})$. The input image, illustrated in Fig. 11(a) consists of vectors, some pointing randomly (noise), and some arranged into a line with a gap (corrupted image). Figure 11(b–c) indicate how well the filters reconstruct the missing part. The output of the transverse filter is both stronger and better oriented to the erased line.

ACKNOWLEDGMENT

The authors acknowledge support from the NSF grant DMR-04-26677 (MK); Portions of this work were done under the auspices of the U.S. Department of

Energy under contract W-7405-ENG-36 and supported by NIH grant AI28433 (HYL).

REFERENCES

1. M. Cross and P. Hohenberg, *Rev. Mod. Phys.* **65**:851 (1993).
2. J. P. Gollub and J. S. Langer, *Rev. Mod. Phys.* **71**:S396 (1999).
3. E. R. Kandel, J. H. Schwartz, and T. M. Jessell, *Principles of Neural Science* (Appleton & Lange, Norwalk, CT, 1991).
4. D. H. Hubel and T. N. Wiesel, *J. Physiol.* **160**:215 (1962).
5. G. G. Blasdel and G. Salama, *Nature* **321**:579 (1986).
6. H. Y. Lee, M. Yahyanejad, and M. Kardar, *Proc. Nat. Acad. Sci. USA* **100**:16036 (2003).
7. N. V. Swindale, *Proc. R. Soc. Lond. B* **215**:211 (1982).
8. N. V. Swindale, *Biol. Cybern.* **66**:217 (1992).
9. F. Wolf and T. Geisel, *Nature* **395**:73 (1998).
10. Constant stirring by sufficiently strong external noise can also lead to dynamic creation and annihilation of pinwheels, but our focus is on evolving fields where the only randomness is in the choice of initial conditions.
11. A. A. Koulakov and D. B. Chklovskii, *Neuron* **29**:519 (2001).
12. F. Wolf, PhD thesis, Univeritt Göttingen, 2000.
13. In fact (as we also found in our analysis of monkey map), not all orientations are equally represented. This type of anisotropy indicates the absence of *any* form of rotation symmetry, and should not be confused with the distinction between full and joint rotation symmetries which is the subject of this article. The former is compatible with rainbow patterns and does not appear to play a role in the stability of pinwheels. We verified this explicitly by numerical simulations in models with a preference for the horizontal direction.
14. J. B. Swift and P. C. Hohenberg, *Phys. Rev. A* **15**:319 (1977).
15. M. C. Cross and P. C. Hohenberg, *Rev. Mod. Phys.* **65**:851 (1993).
16. W. H. Bosking, Y. Zhang, B. Schofield, and D. Fitzpatrick, *J. Neurosci.* **17**:2112 (1997).
17. P. C. Bressloff *et al.*, *Phil. Trans. R. Soc. Lond. B* **356**:299 (2001).
18. The vectorial representation may in fact be appropriate for a more detailed description of cortical maps which includes other aspects of visual input. For example, it is known that V1 cells respond also to the motion of oriented bars.[(19)] Including the direction of motion leads to a more *vectorial* representation.
19. D. Whitney, H. C. Goltz, C. G. Thomas, J. S. Gati, R. S. Menon, and M. A. Goodale, *Science* **31**:878 (2003).
20. B. T. Halperin, in *Physics of Defects, Les Houches Session XXXV, 1980*, R. Balian, M. Kléman, and J.-P. Poirir, eds. (North Holland, Amsterdam, 1981), pp. 813–857.
21. M. Sigman, G. A. Cecchi, C. D. Gilbert, and M. O. Magnasco, *Proc. Natl. Acad. Sci. USA* **98**:1935 (2001).
22. D. J. Field, *J. Opt. Soc. Am. A* **4**:2379 (1987).
23. D. Ruderman and W. Bialek, *Phys. Rev. Lett.* **73**:814 (1994).
24. A. S. Monin and A. M. Yaglom, *Statistical Mechanics*, Vol. 2 (MIT, Cambridge, 1971), pp. 1–58.
25. I. Arad *et al*, *Phys. Rev. Lett.* **81**:5330 (1998).
26. J. H. van Hateren and A. Van der Schaaf, *Proc. R. Soc. London B* **265**:359 (1998).
27. W. T. Freeman and E. H. Adelson, *IEEE Trans. Patt. Anal. Mach. Intell.* **13**:891 (1991).
28. E. Switkes, M. J. Mayer, and J. A. Sloan, *Vision Res.* **18**:1393 (1978).
29. J. D. Pettigrew, T. Nikara, and P. O. Bishop, *Exp. Brain Res.* **6**:373 (1968).
30. B. Chapman and T. Bonhoeffer, *Proc. Natl. Acad. Sci. USA* **95**:2609 (1998).

31. V. Dragoi, C. M. Turch, and M. Sur, *Neuron* **32**:1181 (2001).
32. We confirmed that the spectra become more isotropic as we average over more rotated images. Note that with a matrix $\mathbf{S}_{\alpha\beta}$ obtained from an orientation field, there is no a priori reason for the cross correlations $S_{lt}(\vec{k})$ and $S_{tl}(\vec{k})$ to be zero. We do find that these correlations are small, and also decrease as we average over rotated images.
33. Additional pictures and data are available online from http://www.mit.edu/∼kardar/research/transversality/ModernArt/.
34. C. D. Gilbert and T. N. Wiesel, *J. Neurosci.* **9**:2432 (1989).
35. R. Malach, Y. Amir, M. Harel, and A. Grinvald, *Proc. Natl. Acad. Sci. USA* **90**:10469 (1993).
36. J. I. Nelson and B. J. Frost, *Exp. Brain Res.* **61**:54 (1985).
37. P. Buzás, U. T. Eysel, P. Adorján, and Z. F. Kisvárday, *J. Comp. Neurol.* **437**:259 (2001).
38. Z. Kourtzi *et al.*, *Neuron* **37**:333 (2003).
39. S. B. Laughlin, *Z. Naturf.* **36c**:910 (1981).
40. J. J. Atick and A. N. Redlich, *Neural Comput.* **2**:308 (1990).
41. J. J. Atick, *Network: Comput. Neural Sys.* **3**:213 (1992).
42. Y. Dan, J. J. Atick, and R. C. Reid, *J. Neurosci.* **16**:3351 (1996).
43. W. Bialek, D. L. Ruderman, and A. Zee, in *Advances in Neural Information Processing Systems,* R. P. Lippman, ed. (Morgan Kaufmann, San Mateo, CA, 1991), p. 363.
44. M. Kardar and A. Zee, *Proc. Natl. Acad. Sci. USA* **99**:15894 (2002).
45. For a small patch of the cortex, we can assume a locally linear relation between the visual and cortical coordinates, X and x. At a global level, the map is certainly non-linear. The non-linearity could itself impose rotations in the coordinate frames which complicate the notion of colinearity. Such complications are ignored in the present analysis.
46. C. E. Shannon and W. Weaver, *The Mathematical Theory of Communication* (University of Illinois Press, Urbaba, IL, 1962).